PCCP

Clarifying effects of nanoscale porosity of silicon on the bandgap and alignment: a combined molecular dynamics – density functional tight binding computational study

Journal:	*Physical Chemistry Chemical Physics*
Manuscript ID	CP-ART-02-2023-000633.R2
Article Type:	Paper
Date Submitted by the Author:	26-Apr-2023
Complete List of Authors:	Sundarapura, Panus; Tokyo Institute of Technology, School of Materials and Chemical Technology Manzhos, Sergei; Tokyo Institute of Technology, School of Materials and Chemical Technology; Ihara, Manabu; Tokyo Kogyo Daigaku,

Clarifying effects of nanoscale porosity of silicon on the bandgap and alignment: a combined molecular dynamics – density functional tight binding computational study

Panus Sundarapura, Sergei Manzhos[1], Manabu Ihara[1]

School of Materials and Chemical Technology, Tokyo Institute of Technology, Ookayama 2-12-1, Meguro-ku, Tokyo 152-8552 Japan

Abstract

Porous silicon (pSi) has been studied for its applications in solar cells, in particular in silicon-silicon tandem solar cells. It is commonly believed that porosity leads to an expansion of the bandgap due to nano-confinement. Direct confirmation of this proposition has been elusive, as experimental band edge quantification is subject to uncertainties and effects of impurities, while electronic structure calculations at relevant length scales are still outstanding. Passivation of pSi presents another factor affecting band structure. We present a combined force field – density functional tight binding study of the effects of porosity of silicon on its band structure. We thus perform electron structure-level calculations for the first time at length scales (several nm) relevant to real pSi, and consider multiple nanoscale geometries (pores, pillars, craters) with key geometric features and sizes of real porous Si. We consider the presence of a bulk-like base with a nanostructured top layer. We show that the bandgap expansion does not trend with the pore size but with the size of the Si framework. Significant band expansion would require features of silicon (as opposed to pore sizes) as small as 1 nm, while the nanosizing of pores does not induce gap expansion. We observe a graded junction-like behavior of the bandgap as a function of Si feature sizes as one moves from the bulk-like base to the nanoporous top layer.

Keywords: solar cell, tandem solar cell, porous silicon, molecular dynamics, density functional tight binding

[1] Authors to whom correspondence should be addressed. E-mail: Manzhos.s.aa@m.titech.ac.jp (S.M.), mihara@chemeng.titech.ac.jp (M.I.); Tel.: +81-(0)3-5734-3918.

1 Introduction

Porous silicon (pSi) is an important type of materials for the development of solar cells, in particular tandem solar cells. Porosity at the nanoscale is believed to lead to a bandgap expansion, often attributed to nanosizing, as well as to a direct bandgap due to the loss of long-range order,[1,2] resulting in stronger light absorption. The former allows the control of band alignment, enabling for example all-silicon tandem solar cells in which a crystalline silicon layer is responsible for harvesting low energy photons and a pSi layer higher energy photons.[3–5] This is an attractive proposition given the abundance of Si and technological progress that has been achieved in making porous Si.[6–9] Porous silicon is also used in other types of solar cells and in other devices important for energy conversion and storage such as batteries.[10–17] In the all-silicon solar cell, control of the bandgap of the pSi layer is important to optimize the solar cell. It has been estimated that an efficiency of a Si-Si tandem cell can be as high as 41.9% when the pSi layer has a bandgap of 1.7 eV.[18] The origin of the bandgap expansion and its magnitude are, however, still debatable. The experimental determination of the bandgap of pSi is not certain. Optical spectra that are often used for this purpose contain features which could be attributed to gap states due to pore surfaces and lack of passivation thereof.[19,20] There is no clear cutoff absorption energy. The presence of strongly absorbing features in the spectrum (e.g., due to impurities or nanosized features with a direct bandgap) may indicate a seemingly higher onset energy and mask an overall lower bandgap, and it is the latter which is relevant for band alignment. Reported morphologies of pSi include features such as wells, cavities, and pillars.[21–23] The sizes of these features range from 1 nm to several mm. It is the nano-scale which is of interest to the modification of the electronic structure. We note that a nanosized pore does not mean nano-confinement effects which would lead to bandgap expansion – it is the nanoconfinement of the Si framework (supporting relevant electronic states) that is needed to achieve this. The pores of pSi are passivated, often by hydrogen atoms. Other types of passivation, e.g. oxygenation, electrochemical oxidation, nitrogenation, have been reported.[24–27] Passivation also affects the bandstructure. Overall, there is still lack of clarity on the effects of typical porous morphologies and passivation on the bandgap, which are difficult to disambiguate experimentally.

Electronic structure methods allow computing the bandgap directly, disambiguating influences of pore and Si framework sizes and shapes, of passivation, and of any impurities. Such calculations are typically done at the density functional theory (DFT)[28,29] level.

However, pSi presents an intrinsically large scale problem for DFT, as the reproduction of the nanoscale features of real pSi requires models with at least several thousand atoms. While such calculations could in principle be done with DFT, they are not feasible with methods providing a quantitative bandgap such as hybrid functionals,[30–32] and one has to rely on LDA or GGA approximations.[33–35] Available electronic structure calculations of models of pSi are of an unrealistically small scale. For example, Cruz et al.[36] used a tight-binding model, where a cubic-shaped pore of only about 1 nm (side of the cube) was cut out from a 128-atom cubic periodic simulation cell with a side of 22 nm (20% porosity). More recently, Wu and Tang[37] performed GGA DFT calculations on a model with nanopillars and nanowells and reported a gap expansion of up to about 2.1 eV for different degrees of porosity. However, the wells and the pillars were only half a nm in diameter. While some features of pSi can be captured in such models, e.g., transformation of the bandstructure from the indirect to the direct gap type, these models are unrealistically small. It is trivial that once Si features are made small enough one will obtain nanosizing-induced gap expansion, but any gap expansion observed in such small systems (with features on the order of 1 nm) cannot be related to experimentally observed gaps, as experimental structures in which gap expansion was reported have features of several nm length scale.[23,38,39] Electronic structure calculations at that scale are therefore necessary for understanding any gap expansion resulting directly from the nano-porosity.

While large-scale DFT methods exist,[40–42] the reduction in the CPU cost in them is achieved due to additional approximations; moreover, GGA DFT typically used in DFT modeling of materials significantly underestimates the bandgap. While the underestimation of the bandgap can still allow analysis on a trend level, it can be unreliable when band alignment is concerned.[43] The multitude of morphologies and sizes that need to be explored makes calculations even with DFT methods meant for large-scale modeling not routinely feasible. In this situation, density functional tight binding (DFTB)[44–46] is an attractive option for materials where good parameters exist, as is the case for Si and H-passivated Si, where the siband-1-1 Slater-Koster parameter set provides a quantitatively accurate (i.e. more accurate than GGA DFT) bandgap.[47–49] At the scale considered here, DFTB is therefore advantageous not only for the reduced cost of the calculations (about three orders of magnitude vs DFT) but also for accuracy. Silicon and hydrogen-passivated Si also allows accurate force-field based structural optimization.[50–52] In this study, we therefore adopt a combined force field molecular dynamics (MD) – density functional tight binding approach to study the influence of porosity and nanomorphology on the bandgap of silicon. We

compute a variety of structures with nanosized features observed in real pSi. The structures are optimized with MD and the electronic structure calculations are performed with DFTB.

2 Methods

Molecular dynamics simulations were performed in GULP.[53] The Tersoff force field was used.[50–52] Structures were optimized with until the forces on all atoms were below 0.001 eV/Å. Structures optimized with MD were used to perform density functional tight binding (DFTB) simulations. Periodic DFTB[44] calculations were done in DFTB+.[54] Slab models were formed by adding a vacuum layer of at least 20 Å in the z direction. An electronic temperature of 300 K was applied for electronic states occupations smearing to improve convergence. The siband-1-1 Slater-Koster parameter set was used which was previously shown to result in a correct bandgap of silicon and O- and H- containing silicon compounds.[47–49] This parameter set is, however, inaccurate for structure optimization; therefore, MD structures were used. The lattice constant of Si obtained with the force field, at 5.43 Å, is accurate (matching the experimental value of 5.43 Å[55,56]). We confirmed re-optimizing selected MD structures with DFTB using pbc[57,58] parameters which result in a lattice constant of 5.46 Å, as well as with DFT[28,29] (in Quantum Espresso[59] using the PBE functional,[33] PAW[60] pseudopotentials, a 40 Ry plane wave cutoff and a force tolerance of 2×10^{-4} Ry/Bohr) which resulted in a lattice constant of 5.47 Å, that MD structures are accurate enough and do not result in significant changes in the DOS vs structures optimized with other methods.

Nanostructures of different shapes and sizes (shown in the next section) were made by manually removing Si atoms from a large bulk Si supercell to reach the desired shape and then passivated with hydrogens. The passivation was performed in Materials Studio using "update hydrogen" function, which identifies dangling bonds and passivates them with hydrogen atoms. We generated several types of structures: spherical and cubic pores of different sizes, craters of different sizes, and pillars of different heights, diameters, inter-pillar distances, and base thicknesses. Model sizes varied from 337 to 6187 atoms with features varying from one to several nm. The types of the models are shown in Figure 1. For the case of pillars and craters, we also distinguished contributions to the band structures from the base and the pillars and crater walls, by defining different types of Si atoms (copies of Slater-Koster files) for them. As all structures had sizes in excess of 20 Å, the calculations were done at the Γ point. The densities of states were calibrated to have a zero average electrostatic

potential in the middle of the vacuum region: the average (over the lateral dimensions) electrostatic potential was output as a function of the z coordinate (perpendicular to the slab) and its value in the middle of the vacuum region was set as the 0 of the energy axis.

Spherical pore

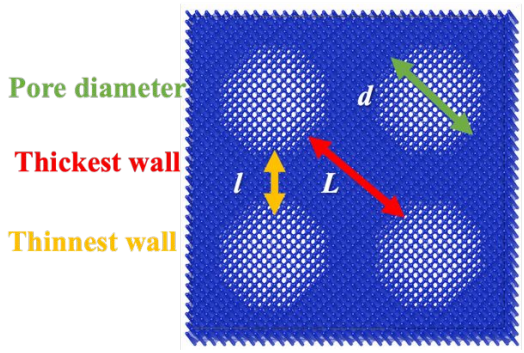

Cubic pore

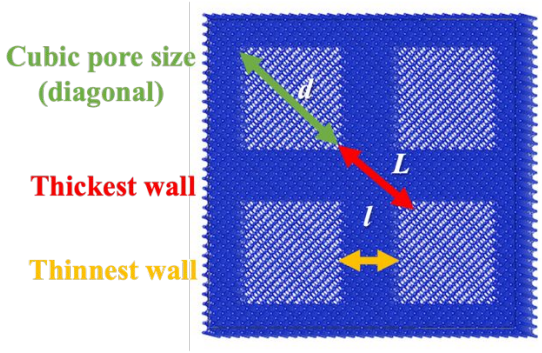

Pillar, side view

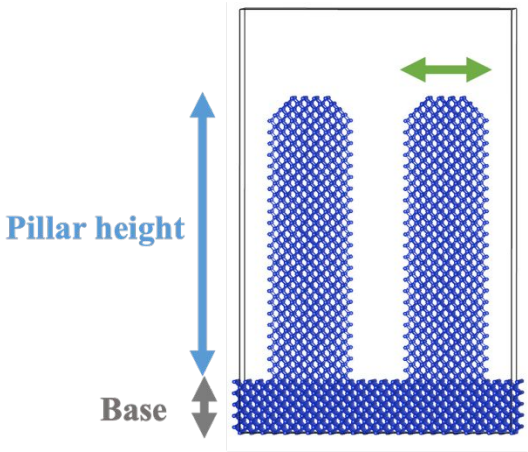

Pillar, top view

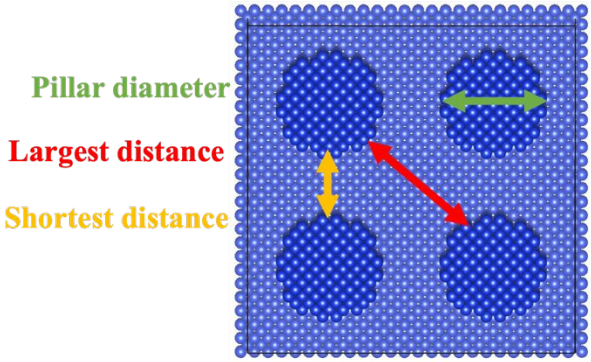

Crater, side view

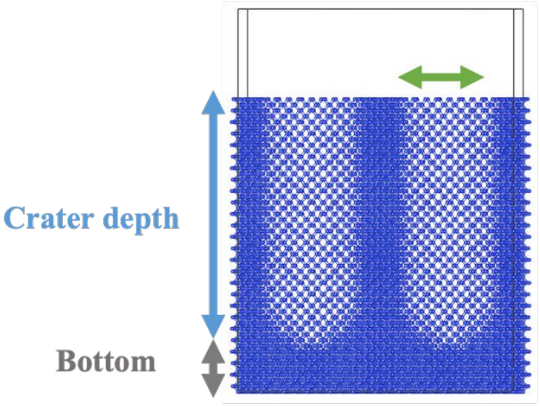

Crater, top view

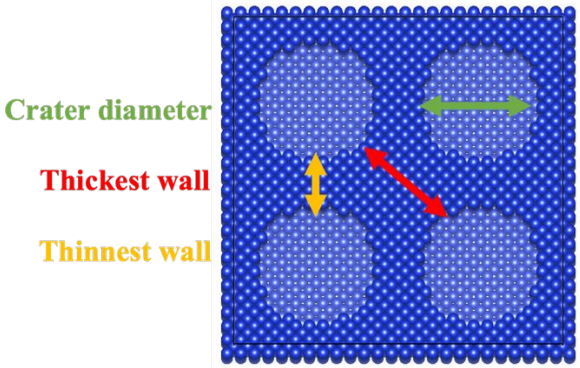

Figure 1: Models generated to simulate porous silicon with different key features: internal sphere and cube models (top row), pillar models (middle row), and crater models (bottom row). 2×2 periodic simulations cells are shown to better demonstrate inter-feature distances. These models were hydrogen-passivated before calculations.

3 Results

The types of the models considered here are shown in Figure 1. These include models with spherical pores of different diameters and with different "wall" thicknesses, pillars with different pillar heights and diameters, base thicknesses, and inter-pillar distances, and craters of different diameters and depths and inter-crater distances ("wall" thicknesses). In addition to spherical pores, cubic pores are also used to better demonstrate the origin of the nanosizing effect.

3.1 Internal Sphere and Cube Models

For the spherical pore models, spheres of different radii were carved in periodic cells of sizes from about 2 to 5 nm. The parameters of the models, including box sizes, numbers of Si and passivating H atoms, pore diameters *d* and resulting inter-pore distances and porosities are listed in in Table S1 of the Supplementary Information. The inter-pore distances are distinguished as follows: the shortest inter-pore distance *l* which is realized by crossing the cubic simulation cell laterally and the largest inter-pore distance *L* which is realized crossing the cubic simulation cell diagonally (in 3D), as shown in Figure 1. These distances define the thickness of the Si framework which ultimately determines the extent of any nanosizing effect. Table S1 also lists the resulting bandgaps as well as band edges. The densities of states are shown in Figure 2 (top). The bandgap of crystalline Si with computational setup of this thesis, which serves as a reference for any nanosizing effects, is 1.07 eV and is in good agreement with the experimental value of 1.12 eV.[61,62] One observes a trend of the bandgap with the size of the model features. The XL3 model represents a case where the pore size is very small while the interpore distance is the largest, with *l* of about 2.9 nm. In this case the bandgap is practically the same as in pure Si, with no gap expansion. The band edges (listed in the SI) of the largest model are also similar to those of crystalline Si. The smallest S models show the largest gap expansion, up to 1.54 eV.

The bandgap expands by slightly lowering the VBM and lifting the CBM simultaneously, as expected for a nanosizing effect. In this case, the trend of the gap is with

the thickness of silicon framework, not the size of the pore. M and L models also show a similar trend. The gap expands even as the pore size is increased, as long as the size of Si features drops.

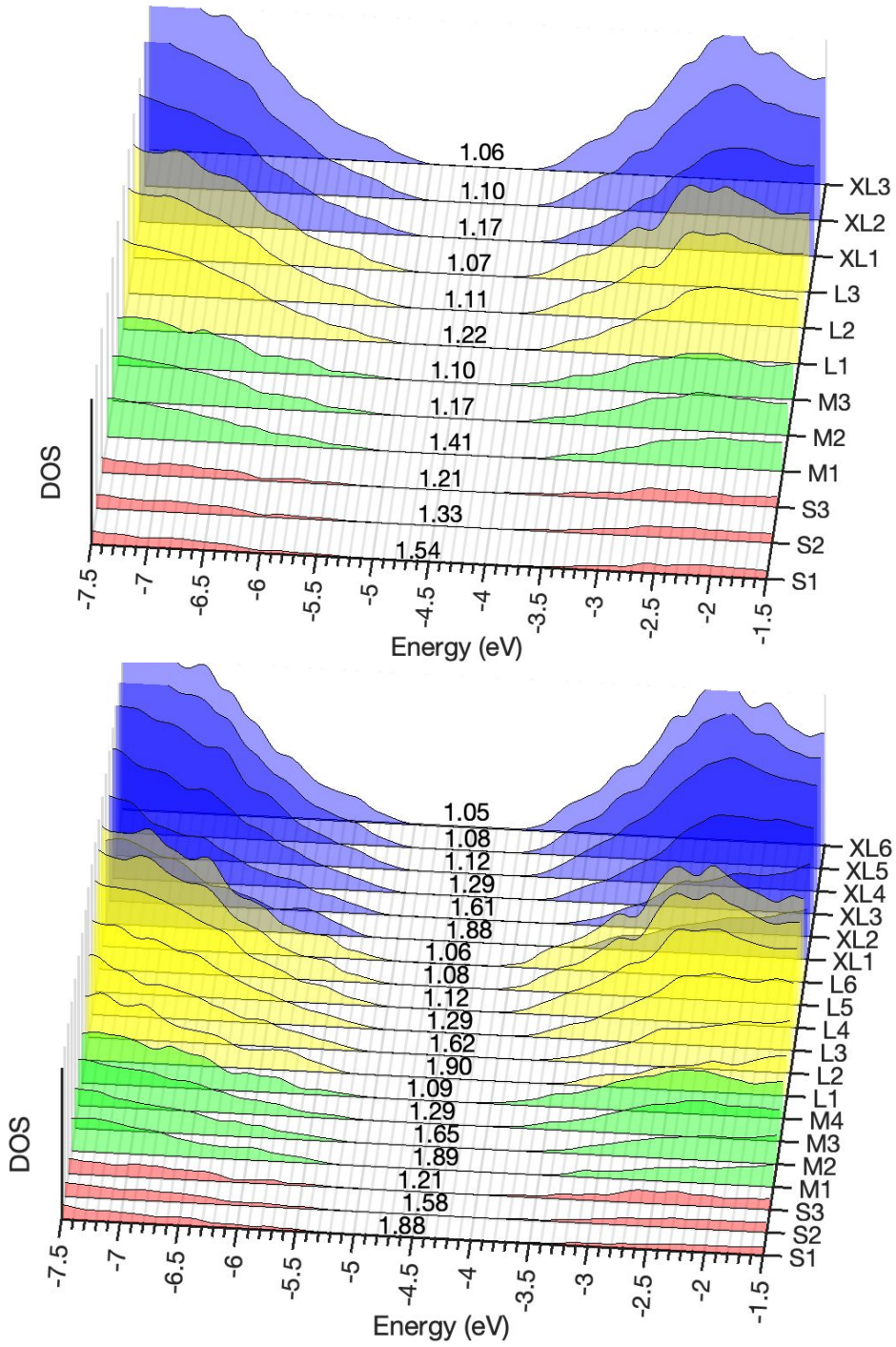

Figure 2: The density of states (DOS) with the bandgap value (in eV) indicated in the middle of each DOS plot. Top: internal sphere models; bottom: internal cube models.

To achieve a significant gap expansion, silicon features need to become smaller than 1 nm. This is because the electronic states of interest, which undergo nano-confining, are localized on Si and not in the pore. To put it simply, it is not the hole of the doughnut that provides a

useful effect. Achieving gap expansion with porosity should therefore aim at controlling the size of Si features rather than the size of the pores or the porosity as such.

To solidify this statement, the calculations on cubic-sized pores are performed, which have a simpler-shaped Si framework than Si with spherical pores, with a clear size parameter – wall thickness. Here, we consider the pore (cube) size, the wall thickness, and the largest Si feature thickness which is a 3D diagonal at the simulation cell vortex. The results are listed in Table S2, and the corresponding densities of states are shown in Figure 2 (bottom). The models with the largest Si features (XL6, L6) also in this case has the band gap and band edges approaching those of crystalline Si, and as Si features get smaller, the gap tends to increase with concomitant decrease of VBM and increase in CBM. We see that Si features need to approach 1 nm for a significant band expansion to occur. Sub-nm features are needed to approach the optimal (from the perspective of a Si-Si tandem solar cell) gap of 1.7 eV. The Si feature sizes in these models required for significant gap expansion are smaller than those experimentally observed here and elsewhere.[63–65] We therefore explore below other morphologies more relevant to the experimental structures.

3.2 Pillar Models

In this type of model, the pillar structure is used to study the effect of 4 silicon features (pillar height, diameter, inter-pillar distance, and base thickness) on its bandgap and band alignment. Previous works reported the bandgap of silicon nanowires depending on the wire (pillar) diameter;[66,67] some having connected the pillar to a base layer, but with a relatively small number of atoms[37] and much smaller scales than the Si feature sizes used in experiments. For the first time, we investigate the effect on the bandgap and band alignment of the other Si pillar features: pillar height, base layer thickness, and the interpillar distance, and at scales relevant to the experiment. The parameters of the models, including simulation cell sizes, numbers of Si and passivating H atoms, pillar height, base layer, pillar diameter, inter-pore distances and porosities are listed in in Table S3.

In Figure 3, the DOS for the pillar models with different combinations of pillar height and diameter and base layer thickness are shown. Only one parameter is varied in each graph, while others are kept constant. Here and below, the DOS of different parts are plotted in different color (pillar: red, base: blue, total: yellow), and the bandgaps computed from the DOS of different parts are also given on the graphs in their respective colors.

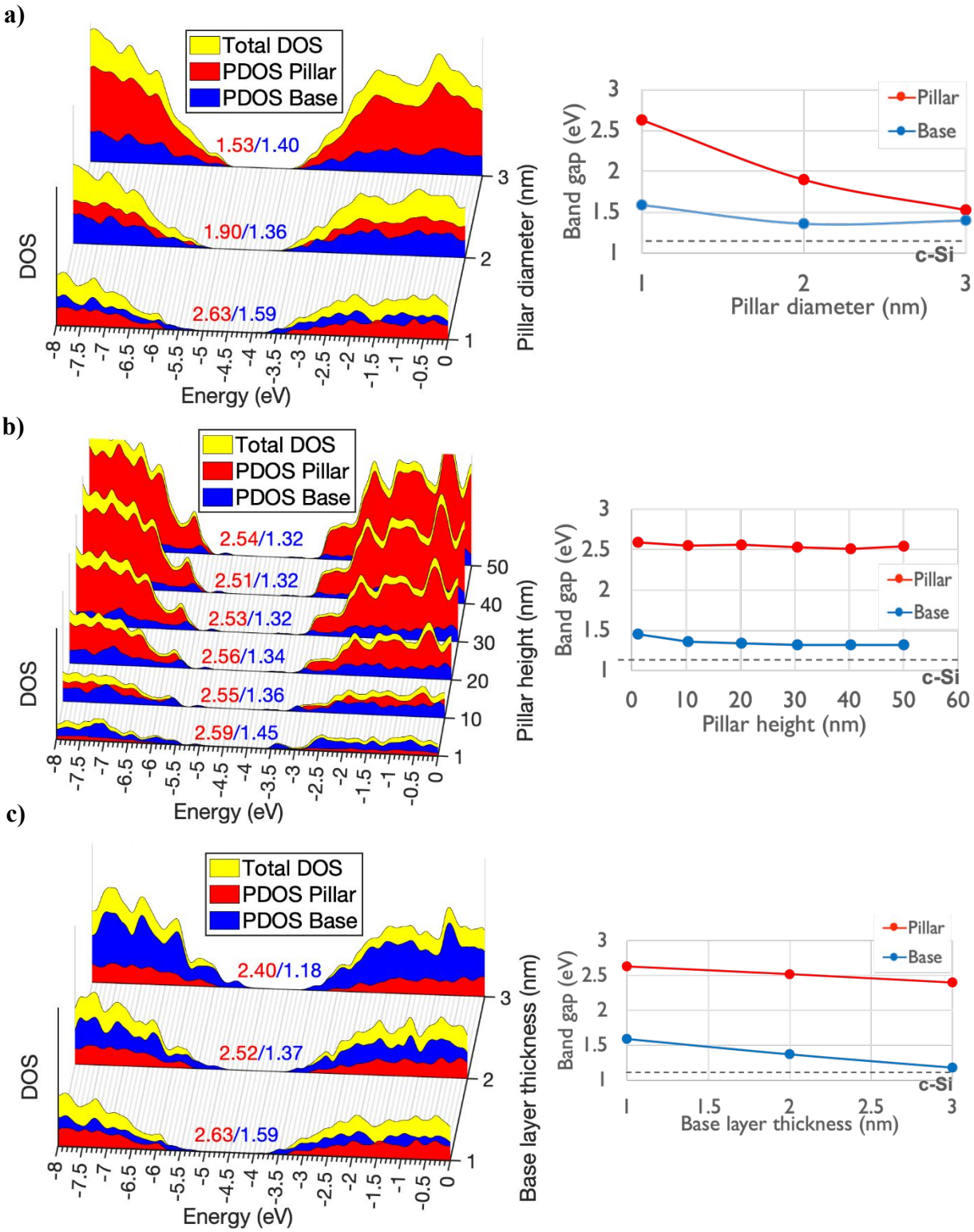

Figure 3: The effects of the pillar features on the bandgap and band alignment; (a) the effect of the pillar diameter; (b) the effect of the pillar height; (c) the effect of the base layer thickness. DOS of different parts are plotted in different color (pillar: red, base: blue, total: yellow), and the gaps computed from the DOS's of different parts are also given in their respective colors.

For the effect of the pillar diameters shown in Figure 3a, the height and the base layer thickness are kept constant at 7 nm and 1 nm, respectively. The key findings from these calculations can be summarized as follows:

1. The bandgap of the pillar part is changed significantly when the pillar diameter is varied. The smaller the pillar, the more confinement effect, the larger the bandgap. The pillar part undergoes a 3-dimensional confinement resulting in a larger effect on the gap expansion compared to a 2-D confinement observed in the base layer part.
2. Pillar models with diameters of 1, 2, and 3 nm result in bandgaps of 2.64, 1.90, 1.53 eV, respectively.
3. The pillar diameter is the key feature that determines the value of the bandgap of the pillar part.

For the effect of the pillar heights shown in Figure 3b, the diameter and the base layer thickness are both kept constant at 1 nm. The key findings from the result are:

1. The difference in height does not significantly affect the value of the bandgap. The pillar diameter is still the main key feature to determine the bandgap.
2. For 1-nm diameter pillar, E_g is about 2.5 eV regardless of the height. The height in this simulation is varied up to 50 nm, without noticeably changing the value of the bandgap.

For the effect of the base layer thickness shown in Figure 3c, the height and the diameter are kept constant at 7 nm and 1 nm, respectively. The key findings are:

1. The increase of the base layer thickness results in the reduction of the bandgap of the base layer towards the bandgap of crystalline silicon (1.07 eV).
    - The bandgap value of each base layer is 1.59 eV, 1.36 eV, and 1.18 eV for 1 nm, 2 nm, 3 nm base layer thickness, respectively.
    - The increase of the base layer thickness also slightly influences the bandgap of pillar. The bandgap of the 1-nm pillar is 2.63 eV, 2.52 eV, and 2.40 eV for 1 nm, 2 nm, 3 nm base layer thickness, respectively.
2. The quantum confinement effect of the base layer results from a 2-D confinement. Therefore, the extent of bandgap expansion is not as significant as the expansion in pillar part where a 3-D confinement effect takes place.

Regarding the effect of the distance between the pillars, the height and the base layer thickness are kept at 10 nm and 1 nm, respectively. In this simulation, the pillar diameters are

also varied in order to see its effect together with the interpillar distances. The distance is varied by changing the lateral size of the simulation cell; the larger the box size, the more distant the pillars; this also significantly increases the number of atoms as the majority of Si atoms are in the base part of the model, which limits the maximum feasible distance. On the other hand, by decreasing the unit box size of the base layer, the distance between pillar can be reduced until the pillars come in contact. The effect on the bandgap energy is shown in Figure 4. The distance, indicated by red arrows in the figures, is defined so as to indicate the size of the silicon feature formed when the pillars touch, in which case the model turns into a crater model.

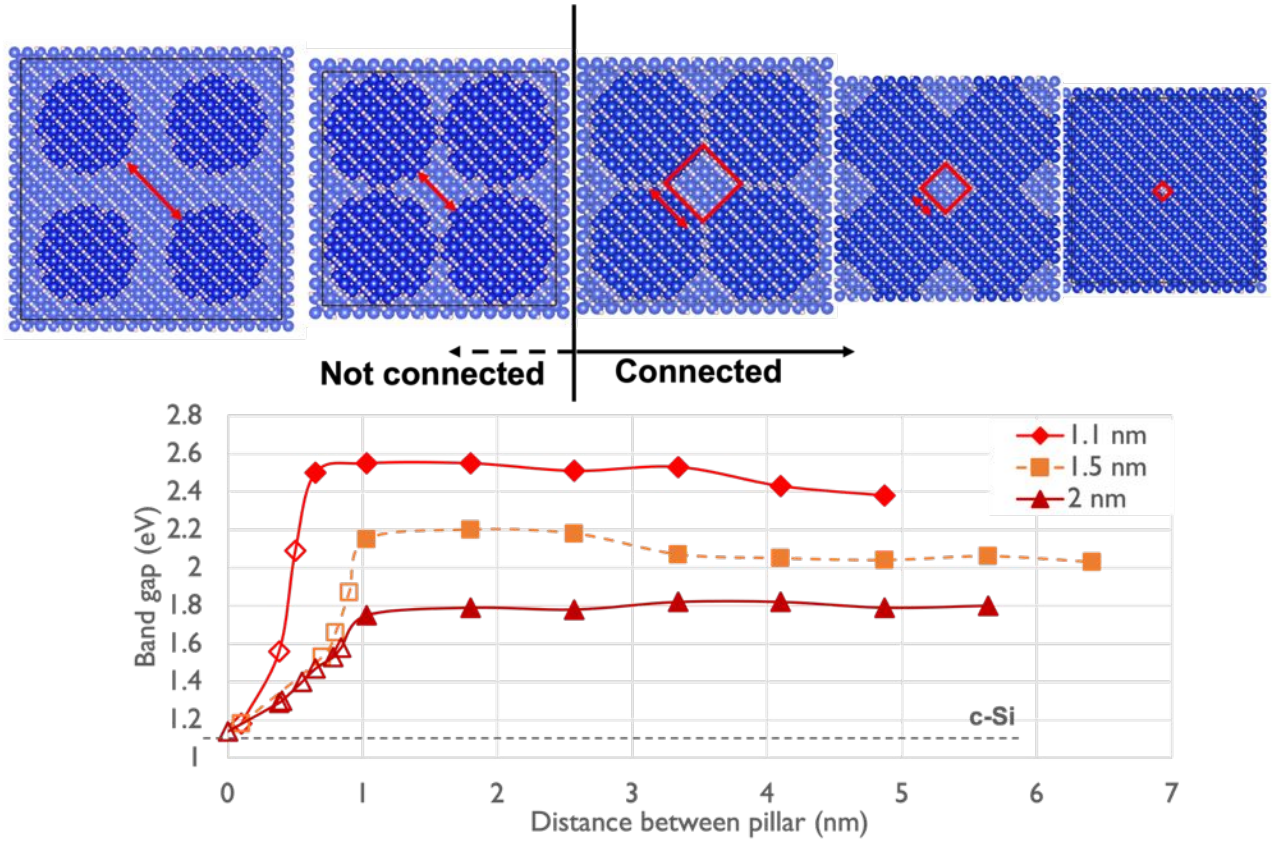

Figure 4: Effect of the distance between the pillars on the bandgap together with the variation of the pillar diameters (for three diameters: 1.1, 1.5, and 2 nm). Top: the pillar models showing the interpillar distance (indicated with red arrow). When these are connected physically, the pillar turns into a crater model, where the connected neighboring pillars form a pore. Bottom: the bandgap values plotted vs the distance between the pillars, where the empty symbols indicate the data when pillars are connected while the filled symbols are for systems where pillars remain separated.

From Figure 4, the key findings are:

1. When the pillars are isolated, the bandgap of the pillar part is determined by the pillar diameter.
2. Only when the pillars are connected, the bandgap starts to decrease towards that of the bulk c-Si (1.12 eV). The more the pillars merge, the smaller the bandgap.
3. The reverse can be observed in the crater model where, as craters are made merge, the model turns into a pillar model; the bandgap increases significantly after the pillars form (explained in the next section).

3.3 Crater Models

In the previous section, the pillar model is used to study the effect of each feature on the bandgap. However, the pillar model does not include pit-like features that can be present in real porous silicon. The crater model is therefore generated in order to get insight into the effect of these features. In this model, 3 crater features are varied: crater depth, the distance between craters which is measured as the size of the thickest part of the inter-crater "wall" (indicated by the red arrow in Figure 1), and crater diameter. Figure 5 shows the DOS and the plotted values of the bandgap vs. sizes of the features. In the same manner as pillar model, the effect of each feature is computed while the other features are kept constant. The parameters of the models, including box sizes, numbers of Si and passivating H atoms, crater depth, base layer thickness, crater diameter, inter-pore distances and porosities are listed in in Table S4.

For the first two effects, a similar trend to that observed with the pillar model could be observed. Firstly, the effect of the crater depth is illustrated in Figure 5a, where the Si thickest wall is kept at 1.92 nm and the bottom layer thickness is kept at 1 nm. It can be seen that the depth of the crater does not affect much the overall bandgap in the same way as the height of the pillar model (Figure 3b). By varying the depth of 4, 6, and 10 nm, the bandgap of the wall part is 1.60, 1.61, and 1.63 eV, respectively, while the gap of the base part is 1.39, 1.43, and 1.45 eV, respectively. This again verifies that the quantum confinement in the height/depth direction is still governed by the thickest part of the Si "wall", which is 1.92 nm thick in this set of simulations and induces a quantum confinement effect leading to a gap expansion of about 1.6 eV. Next, the result of the effect of the thickness of the Si "wall" between the craters is shown in Figure 5b. In this set of simulations, the bottom layer thickness and the crater depth are kept constant at 1 nm and 2.4 nm, respectively. By

changing the lateral size of the simulation cell, the thickest part of the Si wall part can be varied to 1.92, 2.69, and 3.46 nm.

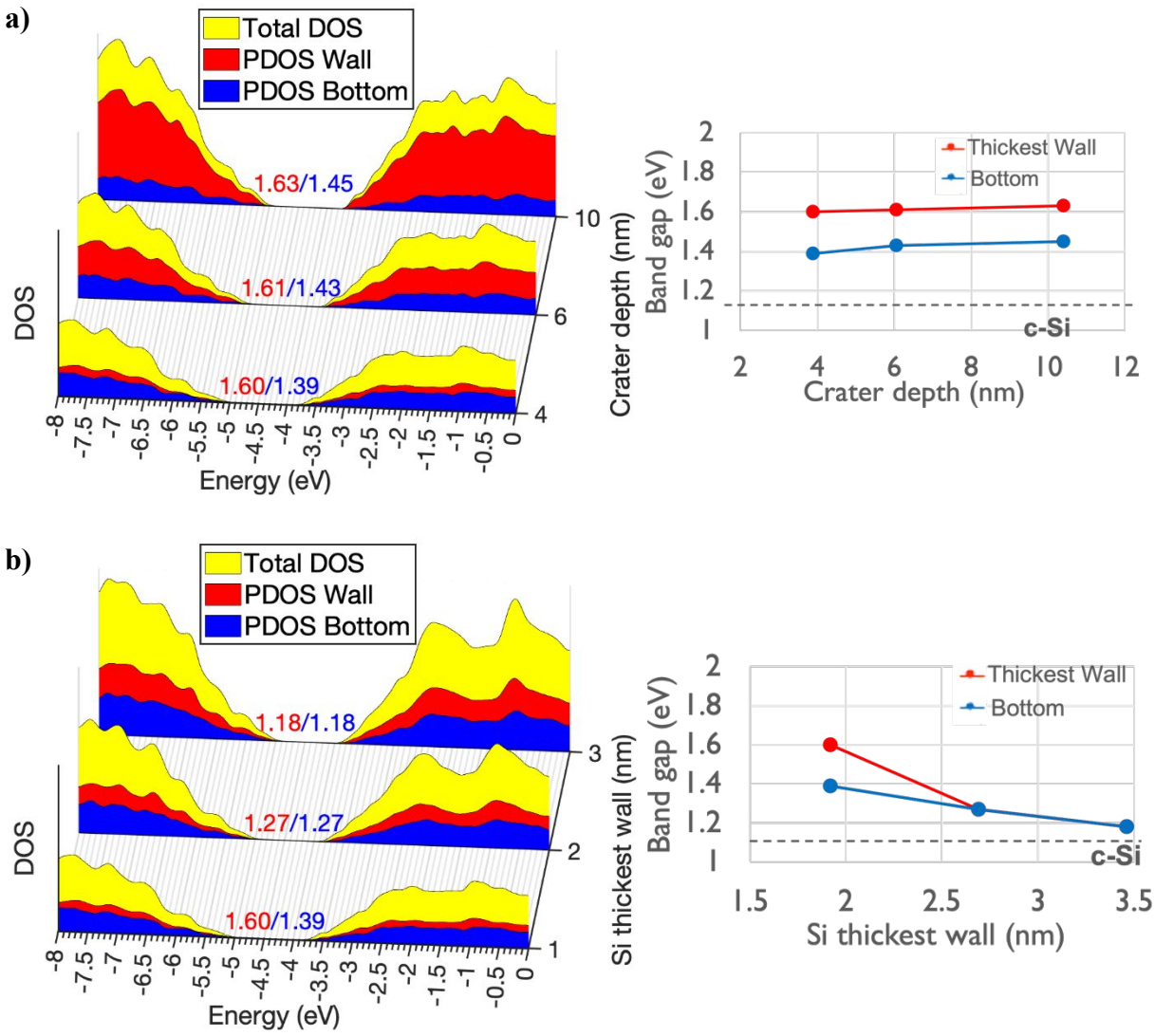

Figure 5: Effects of the silicon features of the crater model on the bandgap and band alignment; (a) effect of the crater depth and (b) effect of the thickness of the Si "wall" between craters. The size of the resulting Si feature is indicated by the red arrow.

It can be observed that as the size the of the Si feature increases, the bandgap decreases accordingly. This verifies that it is the size of the Si feature, rather than the size of the crater, that determines the bandgap of the crater model in the same way as the diameter of the pillar is the determinant for the bandgap of the pillar model. However, the extent of the bandgap expansion is lower than in the pillar model because of the limitation on the geometry of the

crater model in that there is a minimal possible size of the inter-crater Si feature that cannot be made smaller unless craters overlap. Therefore, when the crater model is still maintained, there is a limitation to the extent of quantum confinement effect. The highest bandgap energy obtained is 1.60 eV with a 1.92 nm thick inter-crater Si feature. As the feature becomes larger (with more separated craters), the bandgap converges to that of the bottom part. This indicates that harvesting the quantum confinement effect from the crater-like morphology is more challenging than from nano-pillars, as the Si features must be made smaller than 2 nm to obtain a significant quantum confinement effect.

However, by increasing the crater diameter further, the crater model turns into the pillar model as the craters begin to overlap. This can be clearly seen in the Figure 6 where increasing the crater diameter further decreasing the size of the thus formed pillars. In this case, the opposite effect of the pillar-turn-crater (Figure 4) is observed. After the pillars are isolated (occurred when the crater thickest wall is decreased below 1.54 nm), the bandgap of this Si feature increases dramatically, while the gap of the bottom part remains the same at 1.4-1.5 eV. The highest bandgap expansion is obtained when the isolated pillar has an average diameter size of 0.38 nm, where the bandgap energy is 4.47 eV. It is worth noting that the 0.38 nm pillar in this simulation is rather unrealistic from the experimental perspective.

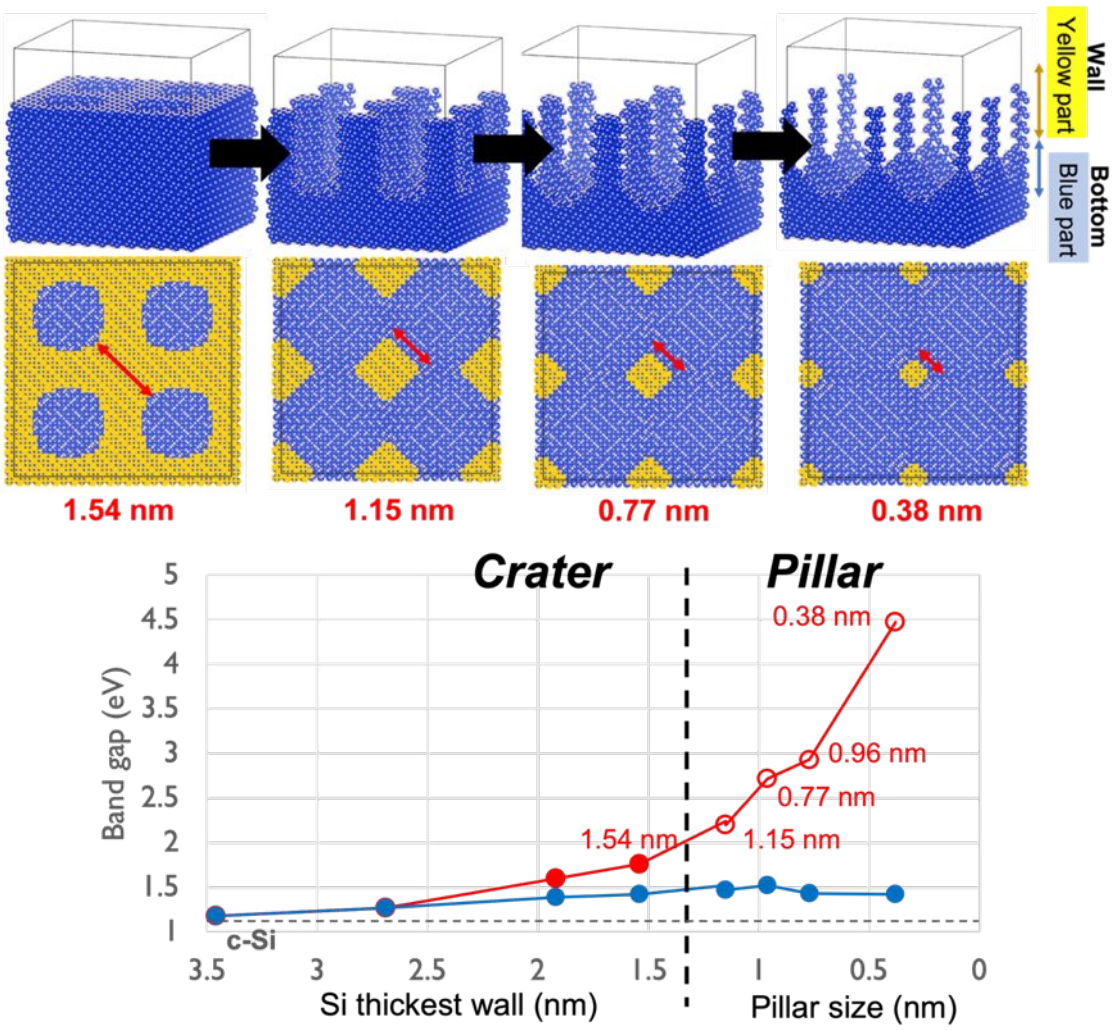

Figure 6: The model showing the transition between the crater model and the pillar model when the size of the inter-crater Si feature is decreased below 1.54 nm so that craters overlap and pillars are formed. Top: the structures of the crater model where the atoms highlighted in yellow indicate the silicon atoms between the craters and the blue atoms are the bottom part. Bottom: the bandgap as a function of the size of the inter-crater Si feature (before pillars are formed) and with an average pillar diameter (when pillars are formed).

3.4 Layer-resolved DOS

The band edges (CBM/VBM) calculated from each model are used to evaluate the band alignment, which is useful for estimation of other solar cell properties like the built-in voltage, maximum open-circuited voltage etc. In the previous sections, the local DOS is used to calculate the difference between bandgap of the pillar and base parts (for the pillar model) and the inter-crater "wall" and the bottom layer parts (for the crater model). In order to

further investigate how the band edges are changed at the interface of PSi/c-Si, we consider DOS in successive layers of the structures.

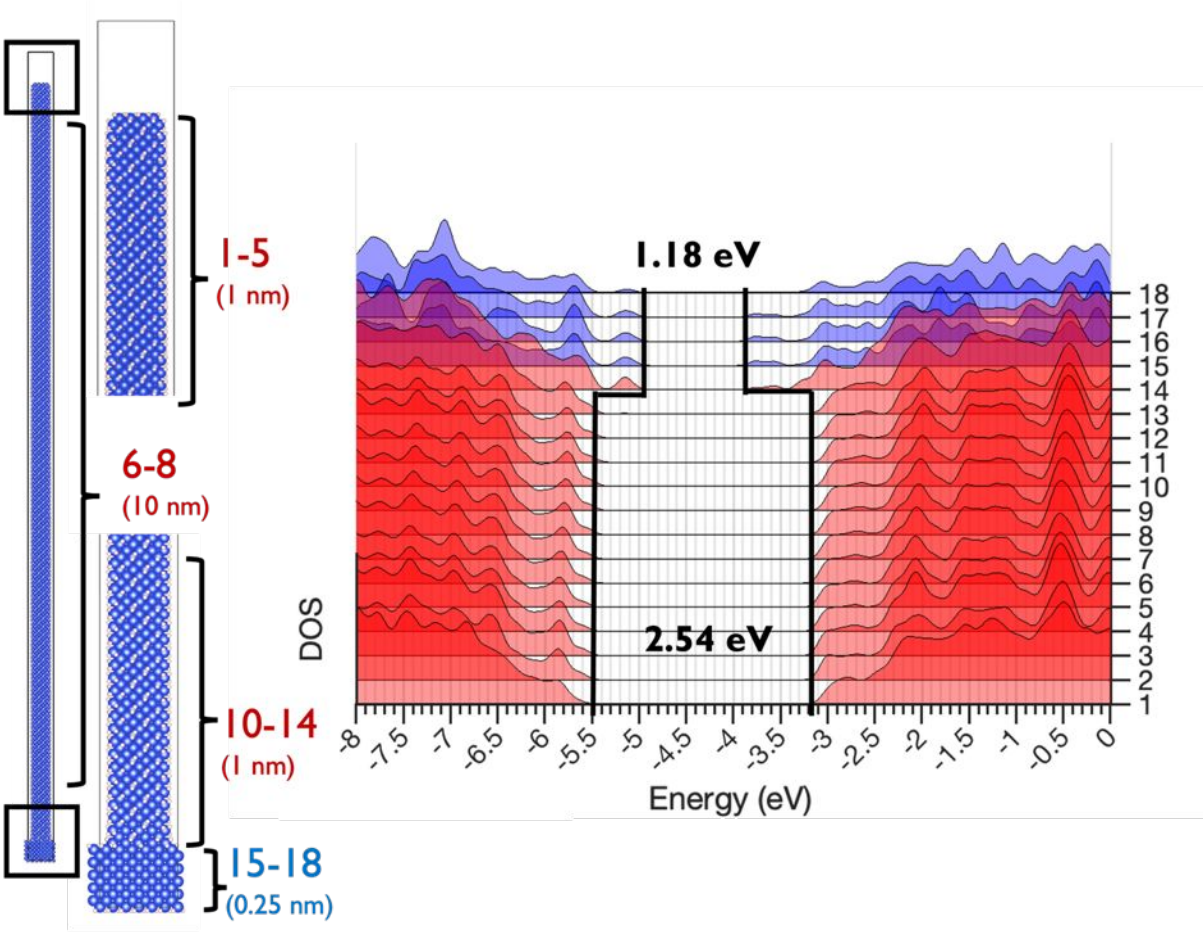

Figure 7: The analysis of the pillar model with a 50-nm height calculated by (left) segmenting each layer of the model; (top right) the local DOS of each segment (blue: base layer segments, red: pillar segments. The thicknesses of the segments are indicated on the left image). The magnitudes of the DOS plots for each layer are made similar for ease of reading. The black line and the number indicate the band edges position and bandgap value

Figure 7 shows such layer-resolved DOS and band alignment in the pillar model. The features of the model are: pillar height of 50 nm, pillar diameter of 1 nm, and base layer thickness of 1 nm. The 18 local DOSs are calculated in each segment of the pillar, where the size of each segments (from the top of pillar) are as follows:

Segment 1-5:	1 nm each	(pillar part)
Segment 6-8:	10 nm each	(pillar part)
Segment 10-14:	1 nm each	(pillar part)
Segment 15-18:	0.25 nm each	(base part)

The blue and red color of the resulting local DOS indicates the pillar and base part, respectively. The key finding from the DOS result can be summarized as follows:

1. From the top down to almost the bottom of the pillar (segments 1-13), the difference in height does not significantly affect the value of the bandgap. The pillar diameter is still the main key feature to determine the bandgap.
2. There is no difference in bandgap energy along the height of pillar; in this case, it is 2.54 eV for a pillar will a 1 nm diameter.
3. Only at the interface between the pillar and the base (segment 14) the local DOS of the pillar is influenced by the base layer and the bandgap immediately drops to the value of base layer (1.18 eV). This affect appears because of the delocalized nature of the orbitals.
4. This kind of drastic change in the bandgap at the interface of the adjoined materials (heterostructure) can be considered an abrupt junction.[68,69]

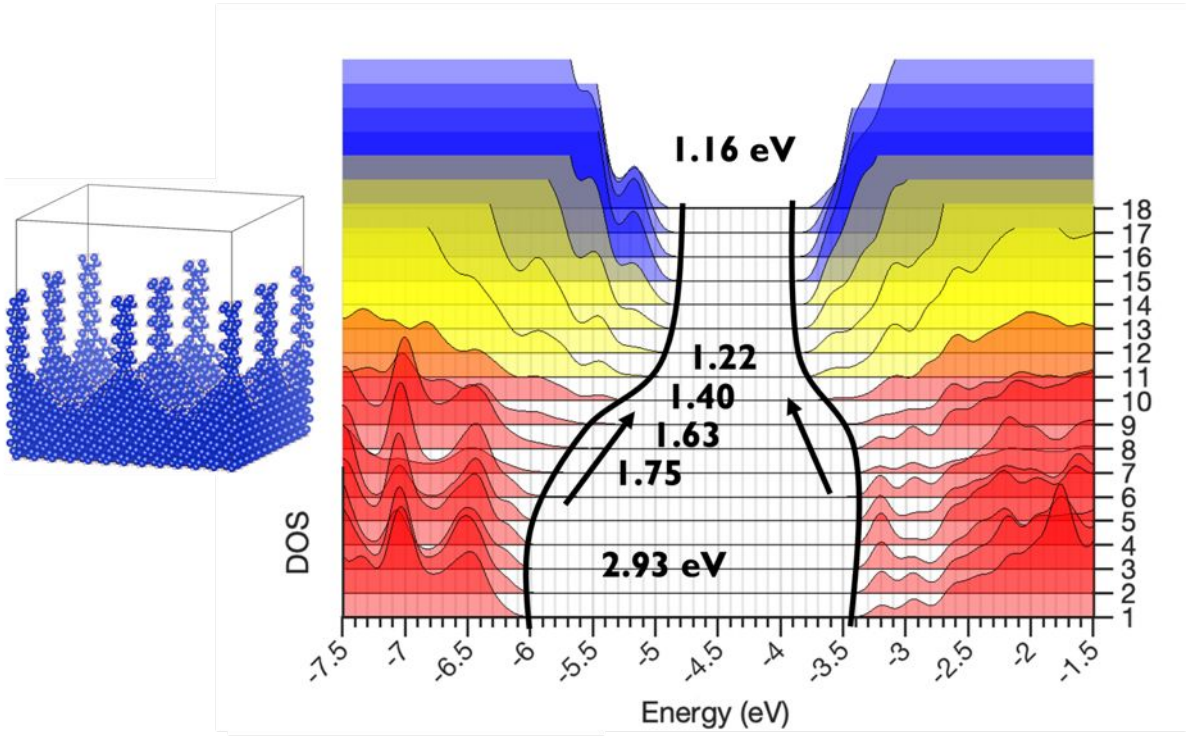

Figure 8: The analysis of the DOS of the crater model with Si pillars (shown in left) calculated by segments; the black line and the number indicates the band edges position and bandgap value.

Figure 8 shows the result of the band alignment of the crater model where the crater diameter is large enough that Si pillars form. This model is intentionally chosen so that one compares the DOS to the pillar model. In the figure, the red color DOS plots are for the Si

pillar part, the yellow color DOS plots are for the bottom of the crater part where the thickness of the Si gradually increases, and the blue color DOS plots are for the base layer part. We observe that the bandgap is constant at 2.93 eV along the pillars and starts to decrease in value as the Si feature thickens towards bottom of the crater. In this case, instead of an abrupt junction like in the pillar model in Figure 7, the bandgap decreases gradually until it reaches the bandgap value of the base layer part (1.16 eV). The band structure formed by this crater model can be considered as a "graded semiconductors".[68,70]

4 Conclusions

We performed a combined molecular dynamics (force field) – density functional tight binding study of the effects of porosity of silicon on its band structure. We considered multiple nanoscale geometries (pores, pillars, craters) with key geometric features and sizes of real porous Si. We considered the presence of a bulk-like base with a nanostructured top layer, mimicking structures observed in real pSi. To the best of our knowledge, we considered for the first time in an electronic structure analysis of pSi length scales relevant to real pSi, which presents an intrinsically large-scale electronic structure problem. The use of DFTB allowed us to consider such length scales while achieving a good bandgap accuracy, which would have been impossible with GGA DFT, due to the existence of an accurate DFTB parameterization for Si.

We confirmed in a direct calculation that the bandgap expansion does not trend with the pore size but with the size of the Si framework. Significant band expansion would require features of silicon (as opposed to pore sizes) as small as 1 nm, while the nanosizing of pores does not induce gap expansion. Achieving gap expansion with porosity should therefore aim at controlling the size of Si features rather than the size of the pores. Among the nanostructures that we considered, pillars are more promising to achieve significant nanoconfinement induced gap expansion, while the extent of it in craters (pits) is limited by the smallest possible size of inter-crater Si features. Both crater and pillar morphologies allow in principle achieving gaps on the order of 1.7 eV, which is a desired value for high-performance Si-Si tandem solar cells. In all cases the gap expansion is accompanied by a stabilization (energy decrease) of the valence band and destabilization (energy increase) of the conduction band. In a solar cell device, Si layers are p- and n-doped, which will push the Fermi level towards the top of the valence band or bottom of the conduction band,

respectively. Because the Fermi level is uniformized across the p-n junction, it is the gap expansion rather than individual VBM and CBM changes (before doping) that is expected to be more important in solar cell applications. We observe a graded junction-like behavior of the bandgap as one moves from the bulk-like base to the nanoporous top layer. The cratered geometry is more apt to form a band alignment of the type of a graded junction. The bandgap changes according to changes in Si feature sizes (such as crater or pillar diameter) in the lateral direction, while the height/depth of the pillars or craters (of fixed diameter) and inter-pillar distance have little effect on the gap. Our results are obtained with a specific computational setup and for the case of Si structures well-passivated by hydrogen. Other types of passivation and defects of crystallinity, which can modify the band structure, were not considered in this work.

5 Author contributions

Panus Sundarapura: Calculations, Methodology, Data analysis, Writing- Original draft preparation, Writing- Reviewing and Editing. Sergei Manzhos: Conceptualization, Methodology, Writing- Original draft preparation, Project administration, Supervision. Manabu Ihara: Conceptualization, Resources, Writing- Reviewing and Editing, Project administration, Supervision.

6 Conflicts of interest

There are no conflicts to declare.

7 Acknowledgements

This work was supported by JST-Mirai Program Grant Number JPMJMI22H1, Japan. S. M. thanks Digital Research Alliance of Canada for access to computational resources.

8 References

1 L. T. Canham, *Appl. Phys. Lett.*, 1990, **57**, 1046–1048.
2 V. Lehmann and U. Gösele, *Appl. Phys. Lett.*, 1991, **58**, 856–858.
3 I. Sagnes, A. Halimaoui, G. Vincent and P. A. Badoz, *Appl. Phys. Lett.*, 1993, **62**, 1155–1157.
4 A. Halimaoui, in *Porous Silicon Science and Technology: Winter School Les Houches, 8 to 12 February 1994*, eds. J.-C. Vial and J. Derrien, Springer, Berlin, Heidelberg, 1995, pp. 33–52.
5 Y. Kurokawa, M. Yano, S. Miyajima and A. Yamada, *Jpn. J. Appl. Phys.*, 2017, **56**, 04CS03.

6 *Handbook of Porous Silicon*, Springer, 2014.
7 O. Bisi, S. Ossicini and L. Pavesi, *Surface Science Reports*, 2000, **38**, 1–126.
8 N. Singh, M. K. Sahoo and P. G. Kale, *Journal of Crystal Growth*, 2018, **496–497**, 10–14.
9 M. K. Sahoo and P. Kale, *Microporous and Mesoporous Materials*, 2019, **289**, 109619.
10 M. S. Almomani, N. M. Ahmed, M. Rashid, K. H. Ibnaouf, O. A. Aldaghri, N. Madkhali and H. Cabrera, *Photonics*, 2022, **9**, 843.
11 Z. Shang, X. Liu, J. Liu, B. Liu, Q. Yu, Z. Lai, N. Ding, S. Zhong and X. Li, *Electrochimica Acta*, 2022, **407**, 139893.
12 G. Huang, J. Han, Z. Lu, D. Wei, H. Kashani, K. Watanabe and M. Chen, *ACS Nano*, 2020, **14**, 4374–4382.
13 S. Li, J. Huang, J. Wang and K. Han, *Materials Letters*, 2021, **293**, 129712.
14 W. An, B. Gao, S. Mei, B. Xiang, J. Fu, L. Wang, Q. Zhang, P. K. Chu and K. Huo, *Nat Commun*, 2019, **10**, 1447.
15 H. Jia, X. Li, J. Song, X. Zhang, L. Luo, Y. He, B. Li, Y. Cai, S. Hu, X. Xiao, C. Wang, K. M. Rosso, R. Yi, R. Patel and J.-G. Zhang, *Nat Commun*, 2020, **11**, 1474.
16 C. W. Jang, D. H. Shin and S.-H. Choi, *Journal of Alloys and Compounds*, 2021, **877**, 160311.
17 R. Ramadan, M. Manso-Silván and R. J. Martín-Palma, *J Mater Sci*, 2020, **55**, 5458–5470.
18 J. P. Connolly, D. Mencaraglia, C. Renard and D. Bouchier, *Progress in Photovoltaics: Research and Applications*, 2014, **22**, 810–820.
19 M. H. Chan, S. K. So and K. W. Cheah, *Journal of Applied Physics*, 1996, **79**, 3273–3275.
20 D. J. Lockwood, *Solid State Communications*, 1994, **92**, 101–112.
21 V. Lehmann, R. Stengl and A. Luigart, *Materials Science and Engineering: B*, 2000, **69–70**, 11–22.
22 X. G. Zhang, *J. Electrochem. Soc.*, 2003, **151**, C69.
23 A. G. Cullis, L. T. Canham and P. D. J. Calcott, *Journal of Applied Physics*, 1997, **82**, 909–965.
24 L. Debarge, J. P. Stoquert, A. Slaoui, L. Stalmans and J. Poortmans, *Materials Science in Semiconductor Processing*, 1998, **1**, 281–285.
25 P. Sundarapura, X.-M. Zhang, R. Yogai, K. Murakami, A. Fave and M. Ihara, *Nanomaterials*, 2021, **11**, 459.
26 T. D. James, A. Keating, G. Parish and C. A. Musca, *Solid State Communications*, 2009, **149**, 1322–1325.
27 Z. Chen and G. Bosman, *physica status solidi (b)*, 1994, **184**, 283–290.
28 W. Kohn and L. J. Sham, *Phys. Rev.*, 1965, **140**, A1133–A1138.
29 P. Hohenberg and W. Kohn, *Phys. Rev.*, 1964, **136**, B864–B871.
30 J. Heyd, G. E. Scuseria and M. Ernzerhof, *J. Chem. Phys.*, 2003, **118**, 8207–8215.
31 J. Heyd, G. E. Scuseria and M. Ernzerhof, *J. Chem. Phys.*, 2006, **124**, 219906.
32 C. Adamo and V. Barone, *J. Chem. Phys.*, 1999, **110**, 6158–6170.
33 J. P. Perdew, K. Burke and M. Ernzerhof, *Phys. Rev. Lett.*, 1996, **77**, 3865–3868.
34 S. H. Vosko, L. Wilk and M. Nusair, *Can. J. Phys.*, 1980, **58**, 1200–1211.
35 J. P. Perdew, K. Burke and Y. Wang, *Phys. Rev. B*, 1996, **54**, 16533–16539.
36 M. Cruz, M. R. Beltrán, C. Wang, J. Tagüeña-Martínez and Y. G. Rubo, *Phys. Rev. B*, 1999, **59**, 15381–15387.
37 X. Wu and Y. Tang, *Surf. Rev. Lett.*, 2018, **25**, 1850045.
38 R. L. Smith and S. D. Collins, *Journal of Applied Physics*, 1992, **71**, R1–R22.
39 S. Dhanekar, S. S. Islam, and Harsh, *Nanotechnology*, 2012, **23**, 235501.

40 L. E. Ratcliff, W. Dawson, G. Fisicaro, D. Caliste, S. Mohr, A. Degomme, B. Videau, V. Cristiglio, M. Stella, M. D'Alessandro, S. Goedecker, T. Nakajima, T. Deutsch and L. Genovese, *J. Chem. Phys.*, 2020, **152**, 194110.

41 A. Nakata, J. S. Baker, S. Y. Mujahed, J. T. L. Poulton, S. Arapan, J. Lin, Z. Raza, S. Yadav, L. Truflandier, T. Miyazaki and D. R. Bowler, *J. Chem. Phys.*, 2020, **152**, 164112.

42 T. Ozaki, *Phys. Rev. B*, 2003, **67**, 155108.

43 W. Li, K. Kotsis and S. Manzhos, *Phys. Chem. Chem. Phys.*, 2016, **18**, 19902–19917.

44 M. Elstner, D. Porezag, G. Jungnickel, J. Elsner, M. Haugk, Th. Frauenheim, S. Suhai and G. Seifert, *Phys. Rev. B*, 1998, **58**, 7260–7268.

45 M. Gaus, Q. Cui and M. Elstner, *J. Chem. Theory Comput.*, 2011, **7**, 931–948.

46 B. Aradi, B. Hourahine and Th. Frauenheim, *J. Phys. Chem. A*, 2007, **111**, 5678–5684.

47 S. Markov, B. Aradi, C.-Y. Yam, H. Xie, T. Frauenheim and G. Chen, *EEE Trans. Elec. Dev.*, 2015, **62**, 696–704.

48 S. Markov, G. Penazzi, Y. Kwok, A. Pecchia, B. Aradi, T. Frauenheim and G. Chen, *IEEE Elec. Dev. Lett.*, 2015, **36**, 1076–1078.

49 S. Markov, C. Yam, G. Chen, B. Aradi, G. Penazzi and T. Frauenheim, in *2014 International Conference on Simulation of Semiconductor Processes and Devices (SISPAD)*, 2014, pp. 65–68.

50 J. Tersoff, *Phys. Rev. B*, 1988, **38**, 9902–9905.

51 F. de Brito Mota, J. F. Justo and A. Fazzio, *Journal of Applied Physics*, 1999, **86**, 1843–1847.

52 A. Yasukawa, *JSME international journal. Ser. A, Mechanics and material engineering*, 1996, **39**, 313–320.

53 J. D. Gale and A. L. Rohl, *Molecular Simulation*, 2003, **29**, 291–341.

54 B. Hourahine, B. Aradi, V. Blum, F. Bonafé, A. Buccheri, C. Camacho, C. Cevallos, M. Y. Deshaye, T. Dumitrică, A. Dominguez, S. Ehlert, M. Elstner, T. van der Heide, J. Hermann, S. Irle, J. J. Kranz, C. Köhler, T. Kowalczyk, T. Kubař, I. S. Lee, V. Lutsker, R. J. Maurer, S. K. Min, I. Mitchell, C. Negre, T. A. Niehaus, A. M. N. Niklasson, A. J. Page, A. Pecchia, G. Penazzi, M. P. Persson, J. Řezáč, C. G. Sánchez, M. Sternberg, M. Stöhr, F. Stuckenberg, A. Tkatchenko, V. W. -z. Yu and T. Frauenheim, *J. Chem. Phys.*, 2020, **152**, 124101.

55 E. Massa, G. Mana, U. Kuetgens and L. Ferroglio, *New J. Phys.*, 2009, **11**, 053013.

56 P. Becker, P. Scyfried and H. Siegert, *Z. Physik B - Condensed Matter*, 1982, **48**, 17–21.

57 A. Sieck, Th. Frauenheim and K. A. Jackson, *Phys. Stat. Sol. (b)*, 2003, **240**, 537–548.

58 C. Köhler, Z. Hajnal, P. Deák, T. Frauenheim and S. Suhai, *Phys. Rev. B*, 2001, **64**, 085333.

59 P. Giannozzi, S. Baroni, N. Bonini, M. Calandra, R. Car, C. Cavazzoni, D. Ceresoli, G. L. Chiarotti, M. Cococcioni, I. Dabo, A. D. Corso, S. de Gironcoli, S. Fabris, G. Fratesi, R. Gebauer, U. Gerstmann, C. Gougoussis, A. Kokalj, M. Lazzeri, L. Martin-Samos, N. Marzari, F. Mauri, R. Mazzarello, S. Paolini, A. Pasquarello, L. Paulatto, C. Sbraccia, S. Scandolo, G. Sclauzero, A. P. Seitsonen, A. Smogunov, P. Umari and R. M. Wentzcovitch, *J. Phys.: Condens. Matter*, 2009, **21**, 395502.

60 P. E. Blöchl, *Phys. Rev. B*, 1994, **50**, 17953–17979.

61 P. J. Collings, *American Journal of Physics*, 1998, **48**, 197.

62 G. G. Macfarlane, T. P. McLean, J. E. Quarrington and V. Roberts, *Phys. Rev.*, 1958, **111**, 1245–1254.

63 R. Herino, G. Bomchil, K. Barla, C. Bertrand and J. L. Ginoux, *J. Electrochem. Soc.*, 1987, **134**, 1994.

64 M. I. J. Beale, J. D. Benjamin, M. J. Uren, N. G. Chew and A. G. Cullis, *Journal of Crystal Growth*, 1985, **73**, 622–636.
65 Y. Kanemitsu, H. Uto, Y. Masumoto, T. Matsumoto, T. Futagi and H. Mimura, *Phys. Rev. B*, 1993, **48**, 2827–2830.
66 M. Nolan, S. O'Callaghan, G. Fagas, J. C. Greer and T. Frauenheim, *Nano Lett.*, 2007, **7**, 34–38.
67 F. Sacconi, M. P. Persson, M. Povolotskyi, L. Latessa, A. Pecchia, A. Gagliardi, A. Balint, T. Fraunheim and A. Di Carlo, *J Comput Electron*, 2007, **6**, 329–333.
68 E. F. Schubert, *Light-Emitting Diodes*, Cambridge University Press, Cambridge, 2nd edn., 2006.
69 F. Capasso and G. Margaritondo, Eds., *Heterojunction band discontinuities: physics and device applications*, North-Holland, 1987.
70 E. F. Schubert, L. W. Tu, G. J. Zydzik, R. F. Kopf, A. Benvenuti and M. R. Pinto, *Applied Physics Letters*, 1998, **60**, 466.